Réunion de printemps de la Société Suisse de Physique = Frühjahrstagung der Schweizerischen Physikalischen Gesellschaft = Spring meeting of the Swiss Physical Society

Autor(en): **[s.n.]**

Objekttyp: **AssociationNews**

Zeitschrift: **Helvetica Physica Acta**

Band (Jahr): **70 (1997)**

Heft Sep. 1

PDF erstellt am: **22.09.2024**

Réunion de Printemps de la Société Suisse de Physique

Frühjahrstagung der Schweizerischen Physikalischen Gesellschaft

Spring Meeting of the Swiss Physical Society

February 27 and 28, 1997

Neuchâtel, Switzerland

Helv. Phys. Acta 70, Separanda 1 (1997) S1 – S2
0018-0238/97/0100S1-02 $ 1.50+0.20/0

Helvetica Physica Acta

High resolution resonant photoemission of Ce-based materials

M. Zacchigna[1], J. Almeida[1], C. Crotti[2], M. Grioni[1], S. La Rosa[3], B. Malaman[4], G. Margaritondo[1], D. Malterre[4], I. Vobornik[1].

[1] *IPA-EPFL, CH-1015 Lausanne, Switzerland*

[2] *IMAI, Padriciano 99, I-34012 Trieste*

[3] *Sincrotrone Trieste, I-34012 Trieste*

[4] *Universitè H. Poincarè 54506 Vandoeuvre, France.*

We have exploited the resonant enhancement of the Ce 4f cross section around 120 eV to investigate the nature of the 4f states in $CePd_3$ and CeSb. Our results are qualitatively consistent with the predictions of the Anderson Impurity Model. In $CePd_3$ our high resolution spectra reveal the characteristic many-body spectral features near the Fermi level.

Many metallic cerium compounds exhibits an unusual behaviour due to the strongly correlated and partially delocalized nature of the $4f$ electrons. This "Kondo phenomenology" and the dependence of the physical properties on the hybridization between $4f$ and conduction electrons are described by the Anderson Impurity Model (A.I.M.)[1]. Here we report an high-resolution investigation of the spectral properties of two very different Ce-based materials. $CePd_3$ is a typical Kondo system, with an estimated Kondo temperature $T_K \sim 300K$. CeSb is characterized by a magnetic ground state ($T_N = 17K$), with little evidence for a Kondo effect. According to the AIM, and to a well-established but recently challenged [2] experimental trend, large differences can be expected in the $4f$ spectral functions of these two systems [3].

Photoelectron spectroscopy (PES) is potentially a very direct probe of the $4f$ spectral function, but separating the $4f$ signal from that of states of different orbital symmetry is often quite difficult. This difficulty can be overcome by tuning the photon energy at the $4d-4f$ threshold, near 120 eV, where the $4f$ photoionization cross section is resonantly enhanced. The use of this $4f$ "giant resonance" is not new, but only recently has it been possible to acquire PES spectra at these photon energies with sufficiently high energy resolution to observe the expected fine structure of the $4f$ spectrum. High resolution PES data ($\Delta E \leq 40\ meV$) have been acquired at the VUV Photoemission Beamline of the ELETTRA storage ring. Clean surfaces of the polycrystalline samples have been prepared by scraping at a base pressure of 1×10^{-10} torr, and PES spectra have been collected at $T = 35K$.

Fig. 1 presents a comparison between on and off- resonance spectra (at 120 and 110 eV respectively) for $CePd_3$. The lineshape dramatically changes with photon energy, and the $4f$ signal is readily identified around -1.2 eV and near E_F. The photon energy dependence of the intensity of the feature at -1.2 eV shows a characteristic Fano profile (solid line).

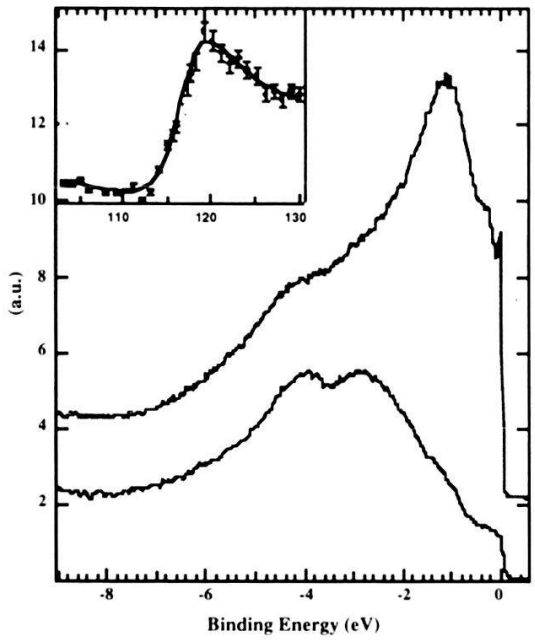

fig.1 Comparison between on-resonance (top) and off-resonance (bottom) spectra for $CePd_3$. Inset: photon energy dependence of the on-resonance spectrum of CeSb.

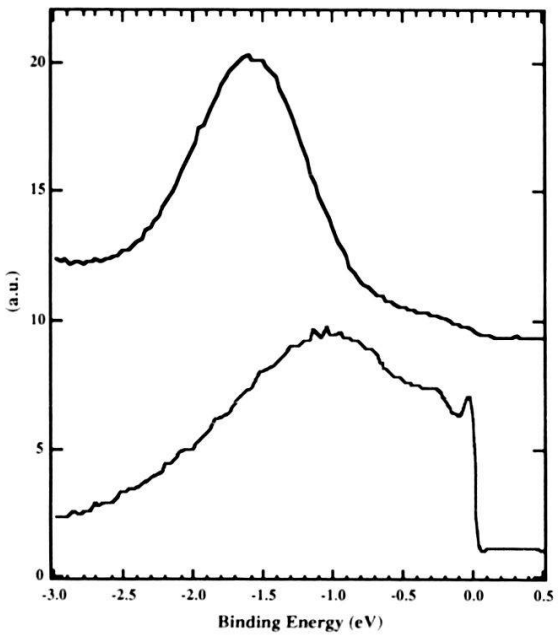

fig.2 Comparison between on-off resonance difference spectra of CeSb (top) and $CePd_3$ (bottom).

In fig. 2 we compare the 120 eV-110 eV difference spectrum of $CePd_3$, which represents to a good approximation the $4f$ signal, with the on-resonance spectrum of CeSb. The CeSb spectrum is dominated by the ionization (f^0) peak at -1.7 eV, while the emission near E_F is vanishingly small. In $CePd_3$, the f^0 peak is found at -1.2 eV, and considerable emission is observed at lower binding energy. The features at E_F and at -0.3 eV represent the tail of the mostly unoccupied Kondo resonance, and a spin-orbit satellite. The observed spectral differences are qualitatively consistent with the predictions of the AIM and support the existence of scaling in the spectral properties of Ce-based materials [1]. From a methodological point of view, these results prove that resonant photoemission can be successfully performed with high energy resolution to yield a very clear image of the $4f$ states in Ce materials.

[1] D. Malterre, M. Grioni and Y. Baer,"Advances in Physics," **45**, 299-348 (1996)

[2] J. J. Joyce et al., "Phys. Rev. Lett.," **68**, 236 (1992).

[3] M. Grioni et al., "Phys. Rev. B.," **55**, 2056 (1997).

Helv. Phys. Acta 70, Separanda 1 (1997) S3 – S4
0018-0238/97/0100S3-02 $ 1.50+0.20/0

Helvetica Physica Acta

Tridimensional Characterization of Voids in Self-Annealed Implanted Silicon Using Electron Holography

C. Beeli [a], G. Matteucci [b], A. Migliori [c], G Lulli [c] and P.G. Merli [c]

[a] Centre Interdépartemental de Microscopie Electronique
Ecole Polytechnique Fédérale de Lausanne, CH-1015 Lausanne, Switzerland
[b] Department of Physics, University of Bologna and Istituto Nazionale per la Fisica della Materia
V/le B. Pichat 6, I-40127 Bologna, Italy
[c] CNR - Istituto LAMEL, Via P. Gobetti 101, I-40129 Bologna, Italy

The characterization of defects produced during self annealing implantation of P^+ ions in silicon is of great interest for the realization of good quality p-n junctions in silicon and to understand the peculiarity of beam-solid interactions occurring during implantation performed under conditions of extremely high current and power density [1-4]. High-resolution electron holography is employed here to study the three-dimensional configuration of sphere-like cavities obtained by 100 keV P^+ ion bombardment of a silicon wafer using a beam with a power density of 15 W/cm^2, respectively 27 W/cm^2 for 4 sec. Phase difference amplification techniques have been used to obtain maps in which the electron phase distribution indicates the thickness contours. From these maps a qualitative topography of the cavity shape as well as measurements of its depth variations are obtained. Electron holography can also be employed to display the various different internal geometries that a void structure can assume.

The study of defects in silicon is of basic importance for the investigation of processes used in microelectronic device technology. Recently, intentionally introduced defects in the lattice have been used to obtain benefits such as impurity gettering or retardation of dopant diffusion. From this point of view, voids with a size of a few tens of nm have obtained renewed interest due to their potential to getter impurities and point defects [1-4]. We report here on the characterization by electron holography of voids produced during self annealing implantation of P+ ions in Si. It is the aim of this contribution to demonstrate the capability of electron holography to display the 3-dimensional topography of nano cavities as well as to measure quantitatively their total depth.
The electron holograms were recorded with a Hitachi HF-2000 FEG transmission electron microscope operated at 200kV. The phase maps were reconstructed from the holograms with the help of the software HoloWorks 1.0 by E. Völkl [5]. Two differently produced samples were investigated: the first obtained with an ion beam power of 15 W/cm^2 contained spherical voids, while a second sample (implanted with 37 W/cm^2) contained octahedral voids.
Figure 1 presents the phase map of a nearly spherical void with a line scan through its center shown below the phase map. It is evident from the profile of this line scan that this void has a spherical shape. However, initial facetting can be noticed from the straight edges in the outline of the void. This is substantiated by the line scan which displays a linear phase change (arrow in the line scan) near such a straight edge. The total phase shift from the edge to the center measures 2.9 ± 0.2 rad. This corresponds to a depth of 29 ± 2 nm, assuming a mean inner potential of 14.1 V for Si (calculated from X-ray scattering factors of Si) thus proving the spherical shape of the cavity. In Fig. 2 the phase map of an octahedral void in [110]-projection is shown, together with two line scans 1 and 2. Line scan 1 allows to recognize that the lower right corner of the void is actually filled with some material, since the phase increases to a value of +1.8 rad. The second line scan is used to measure the approximate depth of the octahedral void: a phase shift of 1.5 ± 0.2 rad corresponds to a depth of 15 ± 2 nm. This value, according to

statistical observations of plane and cross-sections of the specimen has to be compared to the minor diagonal of the cavity itself. Measured directly on the hologram gives: 12 ± 1 nm. Obviously this hole is partially open due to the ion etching procedure which was used to thin the specimen. Therefore, the material in the lower right corner may have been deposed into the void during the ion etching.

Besides the 3-dim. shape information obtained by electron holography, these two examples have shown the possibility to measure quantitatively the depth of nano cavities with a precision of 2 nm. The measurement also allows to decide whether a particular void is actually empty or not. In a similar way it is possible to use this technique for nanostructured materials in order to distinguish between materials with different mean inner potential.

We are very thankful for support and fruitful discussions with P. Stadelmann. The financial support of the Swiss National Science Foundation is gratefully acknowledged.

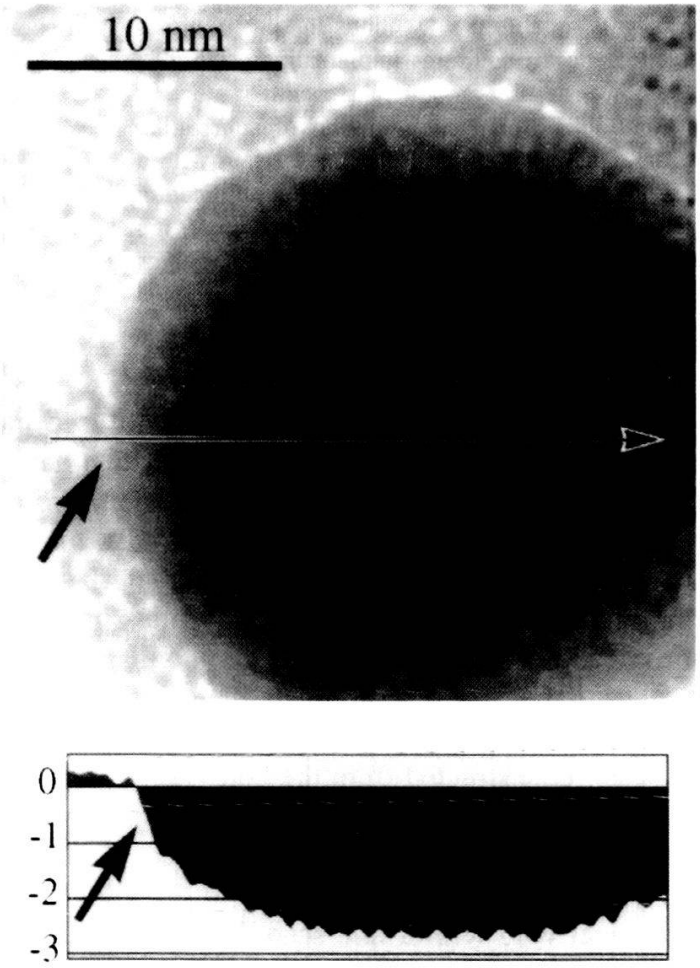

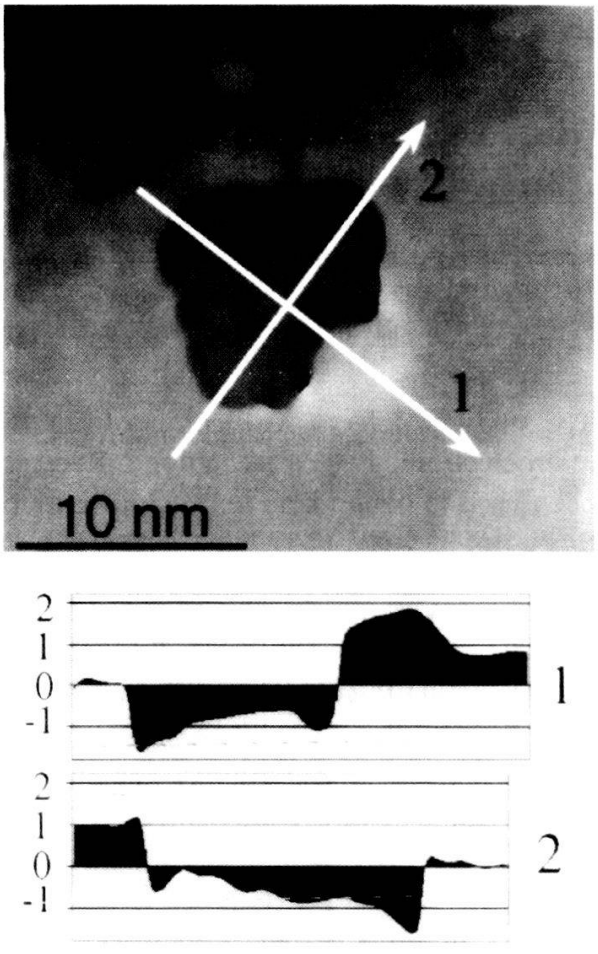

Fig. 1 Phase map of a spherical void, diameter 32 nm. Fig. 2 Phase map of an octahedral void

References

[1] G. Lulli, P.G. Merli, A. Migliori, G. Matteucci, M. Stanghellini, J. Appl. Phys. **68**, 2708(1990)
[2] G. Cembali, P.G. Merli and F. Zignani, Appl. Phys. Lett. **38**, 808 (1981)
[3] G.F. Cembali, M. Finetti, P.G. Merli and F. Zignani, Appl. Phys. Lett. **40**, 62 (1982)
[4] E. Gabilli, R. Lotti, P.G. Merli , R. Nipoti and P. Ostoia, Appl. Phys. Lett. **41**, 967 (1982)
[5] E. Völkl and L. Allard, J. Microscopy **180**, 39 (1995)

Helv. Phys. Acta 70, Separanda 1 (1997) S5 – S6
0018-0238/97/0100S5-02 $ 1.50+0.20/0

Helvetica Physica Acta

Magnetoresistance measurements on single Co nanowires: a direct access to rotation and jumps of the magnetization

J-E Wegrowe, J. Tuaillon, A. Blondel, J. Meier, B. Doudin, J.-Ph. Ansermet
Institut de Physique Expérimentale, EPFL, 1015 Lausanne, Switzerland

The magnetoresistance of individual Co cylinders, 6 μm in length and 150 nm in diameter is interpreted in terms of anisotropic magnetoresistance. Steps of the magnetoresistance are shown, corresponding to switching of fractions of the sample. Statistics of the jumps as a function of temperature have been measured.

Assembly of cylinders with radii below 200 nm, can be obtained by electrodeposition in a porous membrane [1]. For Co wires, in spite of the large shape anisotropy, the magnetization curves reveal a soft magnetic material (Fig.1a). Two reasons can be invoked: first, the polycrystalline nature of the samples and the large magneto-crystalline anisotropy allow transverse magnetization of a fraction of the sample to occur. Second, for large enough radius (150 nm), vortex or domain walls structures are able to take place, also allowing transverse spin configurations to remain even at high field. Recent electron holography experiments confirmed such a picture for the remanent state [2]. The purpose of our work is to show that magnetoresistance measurement can be used to complete our understanding of magnetization reversal.

The anisotropy magnetoresistance (AMR) ratio is proportional to $\langle\cos^2\theta\rangle$ for longitudinal field $H_{//}$ and $\langle\sin^2\theta\rangle$ for transverse field $H_{\perp}$, where the mean value is taken on the current path and θ is the angle between the magnetization and the wire axis [3,4]. From the magnetization measurement giving $M(H)=M_s\langle\cos[\theta(H)]\rangle$, we can deduce an AMR curve if we suppose $\langle\cos^2\theta\rangle = \langle\cos\theta\rangle^2$. This description accounts for the general shape of the measured magnetoresistance curves (Fig 1b).

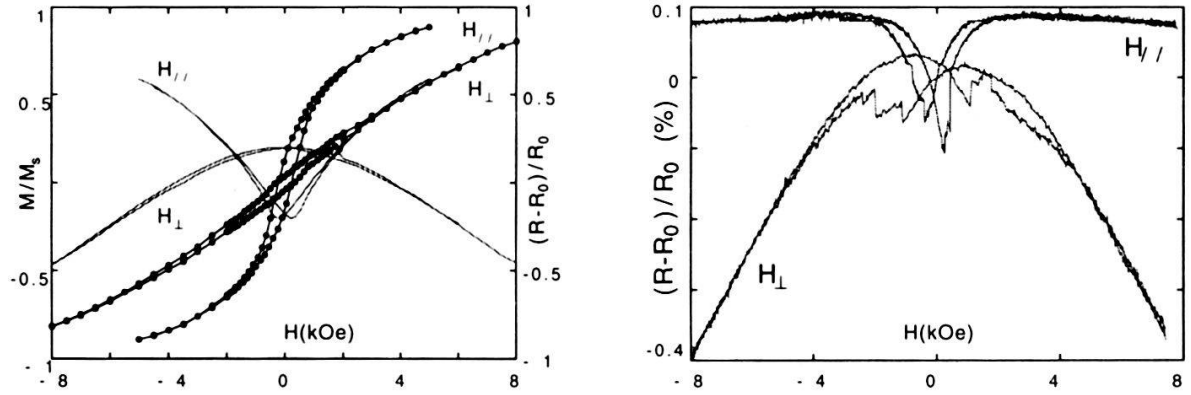

Fig.1 Left: Magnetization measurement of an assembly of Co wires, with the applied field parallel or perpendicular to the wire axis. Shaded lines: typical AMR curve shape deduced from an hypothesis of uniform rotation of the magnetization. Right: magnetoresistance AMR curves, for the two field orientations.

Performing AMR measurements on a single wire, steps of the magnetoresistance can be observed (Fig.2). These steps account for the irreversible part of the AMR. Note the AMR contribution of a switch from a longitudinal position to the opposite longitudinal position is zero and can be observed only if it occurs in separated steps (see Fig2a). Under a sweeping applied field variation, several jumps succeed, and may be superimposed. In order to check that the jumps observed are actually metastable states, the resistivity is measured with fixed field: the applied field is switched rapidly from saturation to a waiting value. The time recording of the resistivity shows that the jump occurring at H=0.457 Oe is due to a relaxation process, and evidences a well defined metastable state (Fig2).

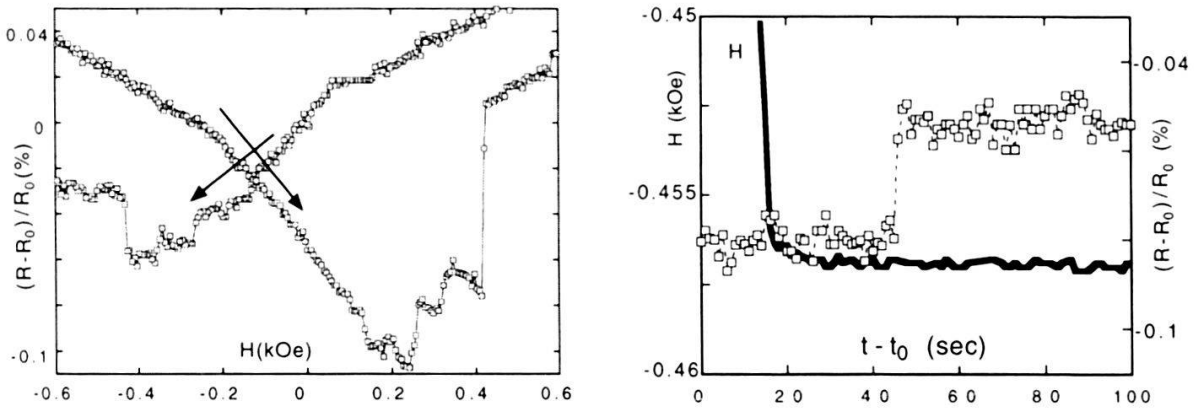

Fig. 2 Left graph: zoom of the central part of a longitudinal AMR hysteresis loop. Right graph: magnetoresistance ratio versus time. Shaded line: applied field versus time, showing that the step of the AMR can spontaneously occur within our filed peak to peak noise of 0.5 Oe. The field is fixed at -0.457 Oe.

When the jump is recorded with a slow varying applied field (1.6 Oe/sec), repetitive measurements allows the histogram of the switching field H_{sw} to be drawn (Fig. 3)[5]. For this sample, the study at several temperatures show that, surprisingly, we do not observe an increase of the fluctuation of the switching field with increasing temperature, but new switching field maxima can occur, revealed by a splitting of the histogram (Fig. 4b). In this case, the increased thermal activation energy has allowed us to reverse the magnetization through another path in the energy landscape. Our measurements can be favorably compared to the study of individual similar nanowires by micro-SQUID sensors [6], sophisticated technique operating in the temperature range 0.03-7K. The width of the histogram we obtain is similar to the one observed with micro-SQUID.

Resistance measurements allowed us to evidence the magnetization reversal of individual sub-micrometric particles. Taking advantage of the large temperature range of experiment, fundamental studies in the perspective of applications in the magnetic storage technology become feasible.

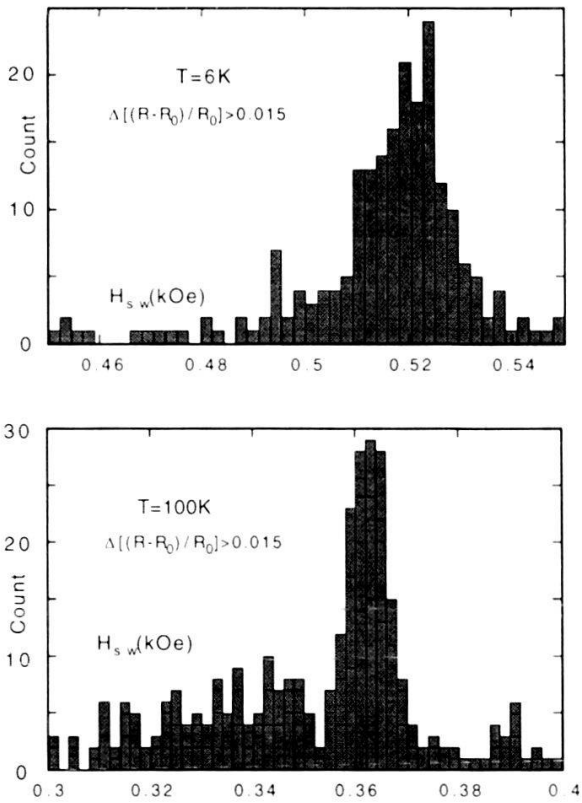

Fig. 3. Histograms of the switching fields, measured at 6 and 100 K.

References

[1] C.R. Martin, Science **266**, 1961 (1994).
[2] C.Beeli, B.Doudin, J.-Ph.Ansermet, P.Stadelmann, J.Mag.Mag.Mater.**164**,77 (1996).
[3] T.R.McGuire, R.I.Potter, IEEE Trans. Magn, **MAG-11**, 1018 (1975)
[4] C.Shearwood, S.J.Blundell, M.J.Baird, J.A.C.Bland, M.Gester, H.Ahmed, H.P.Hughes, J. Appl. Phys. 75 (10) (1994)
[5] Kimin Hong, N. Giordano, J.Phys., Cond.Matt 8,(1996) L.301
[6] W.Wernsdorfer, B.Doudin, D.Mailly, K.Hasselbach, A.Benoit, J.Meier, J.-Ph.Ansermet, B.Barbara, Phys. Rev. Lett. **77**, 1873 (1996).

Helv. Phys. Acta 70, Separanda 1 (1997) S7 – S8
0018-0238/97/0100S7-02 $ 1.50+0.20/0

Helvetica Physica Acta

Light Emission from Si/SiN$_x$ Quantum Wells

D. Grützmacher* R. Morf, H. Auderset, E.F. Steigmeier, and R. Wessicken*

*Micro- and Nanostructures Laboratory, Paul-Scherrer-Institute, 5232 Villigen-PSI, Switzerland
Department for Applied Solid State Physics, Paul-Scherrer-Instiute, 8048 Zürich, Switzerland
*Laboratory for Solid State Physics, Swiss Fed. Institute of Technology, 8093 Zürich, Switzerland

We study the structural and photoluminescence (PL) properties of silicon (Si) quantum well structures, consisting of an either amorphous or crystalline Si layers of 1 to 3 nm thickness, embedded between silicon-nitride layers. After crystallization of the originally amorphous Si layers crytallites with nanometer dimensions are formed. Subsequently passivation by hydrogen yields in strongly polarized PL in the entire visible spectrum. Precise calibration of the spectrometer allows the determination PL efficiencies per incident photon, in absolute units. Our results indicate that optimised structrures may reach PL efficiencies in the percent range.

We studied photoluminescence (PL) properties of a very clean and well-characterized quantum well (QW) system, consisting of an either amorphous or crystalline Si layer of 1 to 3 nm thickness, embedded between silicon nitride layers. The amorphous structures were deposited by plasma enhanced chemical vapor deposition (PECVD) on a Si substrate. To crystallize the Si QW and still preserve the planarity of interfaces in the layer structure, rapid thermal annealing (RTA) was used. The details of the sample preparation are described elsewere [1].

The structural properties of the Si/SiN$_x$ quantum wells were analysed by transmission electron microscopy (TEM) and Raman spectroscopy. Raman spectroscopy clearly indicates a crystallization of the amorphous Si quantum wells after RTA at 1100°C. Moreover the Raman TO phonon line of Si shifts from 515 to 490 cm^{-1} if the Si well widths is decreased from 3 to 1 nm. This shift is expected from model calculation for Si nano clusters [2], therefore these data indicate that the size of the Si nano clusters in our structures is in the same range as the well widths. However, the broadening of the Raman lines may due to a size distribution and particular in the plane of the Si wells, the diameter of the clusters may exceed the well widths. Fig. 1 depicts a TEM cross sectional viewgraph of a single 3 nm Si well embedded in the SiNx after crystallization by RTA. The as deposited amorphous Si well is almost completely crysatllized and small Si clusters (crystals) with varios orientations have been formed. The inset shows an enlargement of a portion of the si well, clearly a crystalline structure is visible.

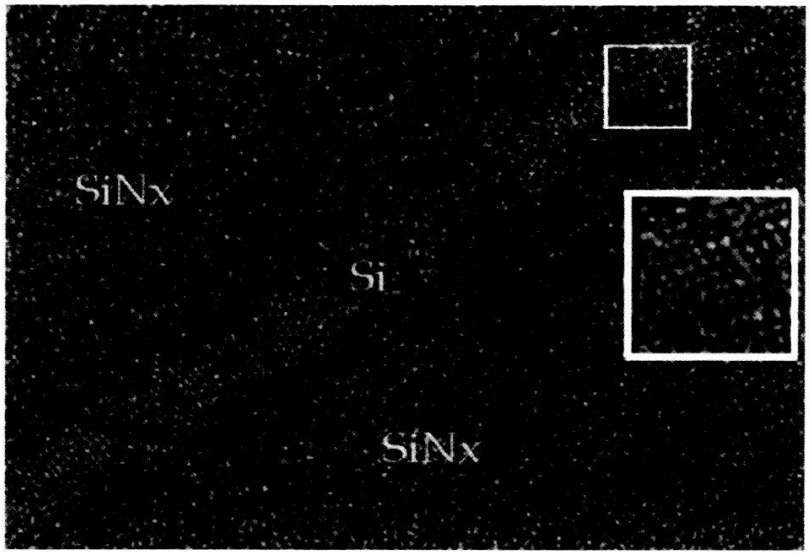

Fig.1: TEM cross section of a 3 nm wide crystallized Si quantum well embedded in SiN$_x$ layers.

Our main results are as follows: Already as deposited, the single QW samples exhibit PL in the entire visible spectrum. After crystallization by RTA and hydrogen-passivation, a significant increase of PL is observed in the blue and green, while red and infrared PL is reduced. The PL, which is strongly polarized, can be observed particularly well if PL is excited and detected at the edge face of the sample. PL intensity is largest when the electric field of both exciting and PL radiation is perpendicular to the Si-QW layer. Measured PL intensities are specified in terms of the spectral PL efficiency $d\eta/d\lambda$. This corresponds to the number of PL photons in a given spectral range, emitted into the hemisphere above the sample, per absorbed excitation photon.

Already as deposited, figure 2a, the QW structure shows a broad PL spectrum throughout the visible range, with somewhat larger intensity for P-polarization for which the electric field has components both in the plane of the QW, as well as normal to it. The cases of P- and S-polarization are shown as full/dotted lines for which either magnetic or electric field of both exciting and PL light is parallel to the QW-layer, respectively. After crystallization by means of RTA, cf. figure b, the PL spectrum is basically shifted towards longer wavelength, with a peak intensity around 650 nm. The polarization effect is much more pronounced than in the „as deposited" stage, with PL above a wavelength of 750 nm fully polarized with magnetic field H parallel to the QW sheet.

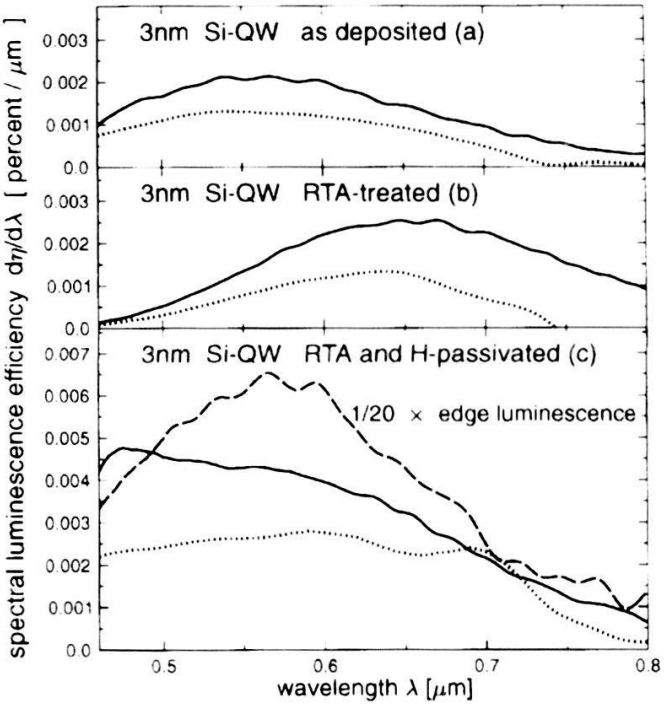

Fig.2: Comparison of PL spectra (300K) for a 3nm wide single quantum well embedded in SiN_x cladding layers (a-c) and a SiN_x film deposited on Si substrate (d). a) as deposited; b) after RTA at 1100°C, c) after hydrogen passivation. Solid lines: E-field of exciting and PL light perpendicular to the QW layer. Dotted lines: E-field parallel to QW.

In figure 2c, we show the PL spectrum for the QW structure in its final stage, after passivation by coating with a hydrogen-rich SiN_X layer. Clarly PL intensity is increased considerably, particularly in the blue, compared to both 'as deposited' (figure 2a) and after RTA crystallization (figure 2b). Indeed, for wavelengths below 500 nm , passivation increases PL intensity by over a factor ten.

The polarization effects observed in figures a-c are actually very significant, if we consider their origin: The difference between PL intensities for the two polarizations must basically arise from the component of the electric field perpendicular to the QW layer, which is non-zero only for P-polarization (i.e. magnetic field parallel to the QW), and scale with its square. Indeed, if PL is excited by illuminating the sample at its edge face significantly higher PL effciency is measured: The dashed line in figure c depicts PL for the polarization in which the E-field of exciting and PL light is perpendicular to the QW layer. Here, PL efficiency is measured per photon incident on the edge face formed by the SiN_X and Si-QW, i.e. a strip of width 190 nm. This probably significantly underestimates the actual effciency, as only some fraction of incident photons are absorbed in the QW. Nevertheless, the PL efficiency is about 30 times larger than in the standard geometry.

We are thus led to the conclusion, that QW structures of the type studied here, should provide more effective light emitting devices than is possible with porous silicon based systems. Provided that PL output can be increased sufficiently, and if carriers can be injected into the Si-QW, our structure, produced by PECVD, may open a viable route for making silicon based electrooptic devices.

Acknoledgement

We like to acknowledge the valuable support of Bernhard Delley, doing model calculations for Si nanoclusters. The financial support by the SPP Optique I and the Swiss National Fonds is gratefully acknowledged.

References

[1] D.A. Grützmacher, E.F. Steigmeier, H. Auderset, R. Morf, B. Delley, R. Wessicken
Mat. Res. Soc. Symp. Proc., *Microcrystalline and Nanocrystalline Semiconductors*
Vol. 358, ed. R.W. Collins, C.C. Tsai, M. Hirose, F. Koch, L. Brus, 1995, p.833

[2] R. Tsu, J. Morais, A. Bowhill
Mat. Res. Soc. Symp. Proc., *Microcrystalline and Nanocrystalline Semiconductors*
Vol. 358, ed. R.W. Collins, C.C. Tsai, M. Hirose, F. Koch, L. Brus, 1995, p.825

Helv. Phys. Acta 70, Separanda 1 (1997) S9 – S10
0018-0238/97/0100S9-02 $ 1.50+0.20/0

Helvetica Physica Acta

MATERIAL ASPECTS OF ZNO TO MAKE SURFACE TEXTURE GROWTH FOR LIGHT TRAPPING FOR THIN FILM SOLAR CELLS

J. A. Anna Selvan, H. Keppner, U. Kroll, J. Cuperus, T. Adatte*, C. Ketterer‡ and A. Shah

Institut de Microtechnique,* Institut de Geologie, Universite de Neuchâtel, ‡CSEM Instruments, CH-2000 Neuchâtel

The efficiency of thin film solar cells can be increased through the process of light trapping by having thin films of *surface-textured* transparent conducting oxides (as a window and back contact), and particularly by using doped Zinc Oxide (ZnO) for this. Apart from aiming at high electrical conductivity and high optical transmission in the visible light range, the growth of ZnO films with textured surfaces is of main interest in the context of thin-film solar cells. In this work, we present the *material aspects of ZnO* that play an important role in growing ZnO films with textured surfaces. The surface texture growth of ZnO under different deposition conditions, by both sputtering and by Chemical Vapour Deposition (CVD), is presented.

A number of depositions have been carried out by the method of sputtering as well as by Chemical Vapour Deposition. For sputtering, a mixture of argon with water vapour was used as the sputtering gas. The target was sintered with 2% Al_2O_3 to obtain electrically conducting films. The substrate temperature, RF power and the ratio of water vapour to the Ar gas were varied and optimised for surface-textured ZnO:Al films. For chemical vapour deposition, B_2H_6 was used as the dopant. Diethyl Zinc and water vapour were allowed to effect a chemical reaction on the substrates. The latter have been kept at a temperature of 150°C. In the second case of CVD 'Boron carrier gas II' was used for doping the ZnO films. These films were characterised to reveal their structural, surface, optical and electrical properties. The material aspects of ZnO to be considered to obtain apropriate surface texture growth were studied.

ZnO belongs to the hexagonal wurtzite structure, generally. It has a tetrahedral co-ordination formed by the sp^3 hybridisation of orbits. In the wurtzite structure, we have alternate Zn and O atoms. With this, the direction of each apex is along the c-axis of the hexagonal system. Hence, it always tries to grow along <0001> direction. Because of this reason, we easily get ZnO films that are <0001> oriented, i.e that have their C- axis perpendicular to the substrate. Since the preferred orientation coincides with one of the crystallographic axes, ZnO has the 'fiber texture'. To avoid confusion between this 'crystallographic texturing' in the bulk of the ZnO thin films and the 'texturing' used for light trapping, the latter will be called 'surface texturing'.

The ZnO films doped with Aluminium and deposited by the method of sputtering showed very high fiber texture orientation along the c-axis. This is the general case when Ar only is used as the sputtering gas. When a mixture of Ar and water vapour were used as the sputtering gas, we have two regions in the deposition parameter space. In the first region the fiber texture nature of ZnO is conserved. This happens at low partial pressure of water vapour. In the second region, we have additional orientations along with the <0001> orientation. This happens at high partial pressure of water vapour. The corresponding surface morphologies show two distinct behaviours. The first one corresponds to a columnar structure with hexagonal faces. This is because of the columns of the hexagonal unit cells that have grown perpendicular to the plane of the substrate. The second one is a granular morphology with rounded grains. This corresponds to the presence of cubic and hexagonal structures of ZnO.

When using the CVD method, one has a broad range of orientation and surface modifications. The ZnO films grown by doping B_2H_6 have preferred orientations along $<11\bar{2}0>$ direction. This is the second lowest index plane of ZnO. Because of the non equilibrium conditions in this method, we get the preferred orientation plane that is different from the lowest index plane, the later being the (0001) plane. In this orientation the c-axis is parallel to the substrate. The surface morphology corresponds to the facets of $(11\bar{2}0)$ planes.

By using 'Boron Carrier gas II' we have further the c-axis orientation parallel, perpendicular and inclined to the substrate.

One of the most important properties to be considered during the growth process is the surface mobility of adatoms. As the films described above show unique differences in their crystallographic orientations, it is possible to obtain the corresponding growth along their low index planes. In other words, by increasing the surface mobility the adatoms can lead to the development of well-defined crystal faces, particularly those of low surface energy (low index planes).

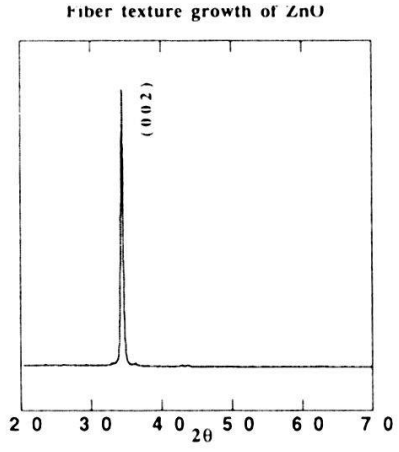

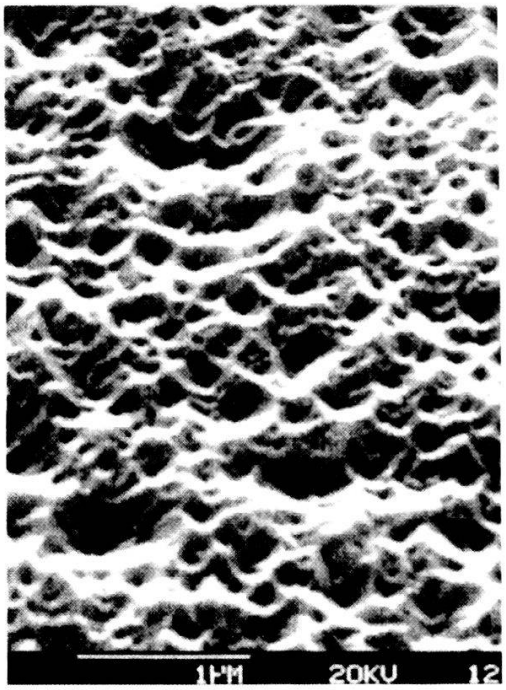

Figures show the equilibrium growth of ZnO and the corresponding surface morphology. The film was grown by the method of sputtering. Here the c-axis of the hexagonal wurtzite structure of the ZnO film is perpendicular to the substrate. The surface mobility, along with the anisotropic reaction of water vapour lead to the growth of surface with hexagons.

The surface mobility could be increased in several ways. In RF sputtering, the RF power plays an important role in making surface textured ZnO films. In CVD, the substrate temperature and the ratio of reacting gases play the decisive role with respect to the surface morphology. With these conditions we could succeed in obtainning 'surface textured' ZnO films with unique surface morphologies.

Particularly for ZnO, another important factor that decides the surface texturing is the hydroxyl group that is dissociated from water vapour. The hydroxyl group can react with ZnO anisotropically along the <0001> direction. In other directions it is in general inert. This anisotropic reaction along with the surface mobility during growth is the key in understanding the process of surface-texturing of ZnO.

We have obtained the ZnO thin films with different surface morphologies by controlling the fiber texture, the surface mobility, and the growth process. We could explain the mechanisms of surface texture growth. Thus, ZnO, being an important material to serve the purpose of electrodes for thin film solar cells can also serve as a successful light-trapping film by the methods mentioned above.

References

[1] J.A.Anna Selvan, H.Keppner and A.Shah Proceedings of MRS spring meeting 1996,san Francisco Vol 426,
[2] J.A. Thronton, J. Vac. Sci. Technol., 11 (1974) 666
[3] Van der DRIFT, Philips Res. Repts 22, 267-288, 1967
[4] J. A. Anna Selvan, H. Keppner, U.Kroll, J. Cuperus, T.Adatte, N. Randall and and A.Shah MRS spring meeting 1997, San Francisco

Helv. Phys. Acta 70, Separanda 1 (1997) S11 – S12
0018-0238/97/0100S11-02 $ 1.50+0.20/0

Helvetica Physica Acta

Compact blue laser based on sum-frequency mixing of laser diodes in $KNbO_3$

D. Fluck and P. Günter
Nonlinear Optics Laboratory, Institute of Quantum Electronics,
Swiss Federal Institute of Technology, ETH-Hönggerberg,
8093 Zürich, Switzerland.

A diode-pumped blue laser is demonstrated by noncritical type I phase-matched sum-frequency mixing in a potassium niobate ($KNbO_3$) crystal. A maximum output power of 25 mW of continuous-wave and diffraction limited radiation at 433 nm is generated in a 6.6 mm long crystal by sum-frequency mixing a 982 nm master-oscillator power-amplifier InGaAs laser diode and a 774 nm AlGaAs laser diode. The blue laser is continuously tuneable over the wavelength range from 431 to 438 nm.

Compact blue lasers are attractive for applications such as optical recording, xerography, lithography, spectroscopy, cytometry, and display systems. Direct second-harmonic and sum-frequency generation (SFG) with near infrared semiconductor laser diodes (LDs) offers the possibility of a robust, compact and reliable blue laser. $KNbO_3$ crystals are very attractive for frequency conversion of near infrared LDs into the blue spectral range due to their high nonlinear optical coefficients and their favourable noncritical phase-matching (PM) configurations.[1] Using the nonlinear optical coefficient d_{32} of $KNbO_3$ tuneable blue light from 415 to 475 nm can be generated by noncritical type I PM sum-frequency mixing (SFM) of radiation at wavelengths in the red (660 - 690 nm) and near infrared (770 - 1100 nm) spectral ranges which are covered by commercially available single-mode AlGaInP, AlGaAs and InGaAs laser diodes. The recent development of master-oscillator power-amplifier LDs with single-mode output powers of up to 2 W in a diffraction-limited beam make this type of laser potentially attractive for SHG and SFG.[2] Efficient SHG with MOPA LDs has recently been demonstrated.[3, 4]

Here we report for the first time, to the best of our knowledge, on SFG using a MOPA LD. In our experiments a MOPA LD (SDL 5762) was used as one of the mixing sources. For an oscillator current of ~250 mA, an amplifier current of ~2.85 A, and an operation temperature of 25.0 °C the output power was 1 W in a nearly diffraction-limited beam ($M^2 \leq 1.3$) of about 2.7 mm widths at a wavelength of 982 nm. A tuneable LD (SDL 8630) was used as the second mixing laser. By scanning the grating angle it is possible to continuously tune the emission wavelength from 768 to 792 nm. For an operation current of 1.8 A the LD provided a maximum output power of about 730 mW in a nearly diffraction-limited beam ($M^2 \leq 1.3$) with a diameter of ~3.5 mm. A telescope consisting of $f_1 = 40$ mm and $f_2 = 30$ mm AR coated lenses was inserted in front of the

tuneable LD to provide a beam with a diameter of ~2.6 mm. The two laser beams were then combined using a dichroic mirror and were focused with a 60 mm, anti-reflection (AR) coated, plan-convex lens to beam waists of about 25 μm in a 6.6 mm long a-cut $KNbO_3$ crystal which was dual-band AR coated at 430 and 860 nm. The crystal was placed in a small oven, mounted on a transverse electric cooler (TEC), and temperature controlled to better than ± 0.1 °C. The SF radiation was collimated with a 30 mm, AR coated lens to provide an output beam with a diameter of about 1.4 mm. A maximum SF power of 25 mW was generated with incident mixing powers of 960 mW from the MOPA LD and of 600 mW from the tuneable LD for an overall normalised conversion efficiency of 4.3 %/W (Fig. 1). The SF output radiation was found to be nearly diffraction-limited ($M^2 \leq 1.1$). It was possible to continuously tune this SF laser from 431 to 438 nm by tuning the temperature of the crystal from 49 to 79 °C and by tuning the wavelength of the AlGaAs LD from 768 to 792 nm.

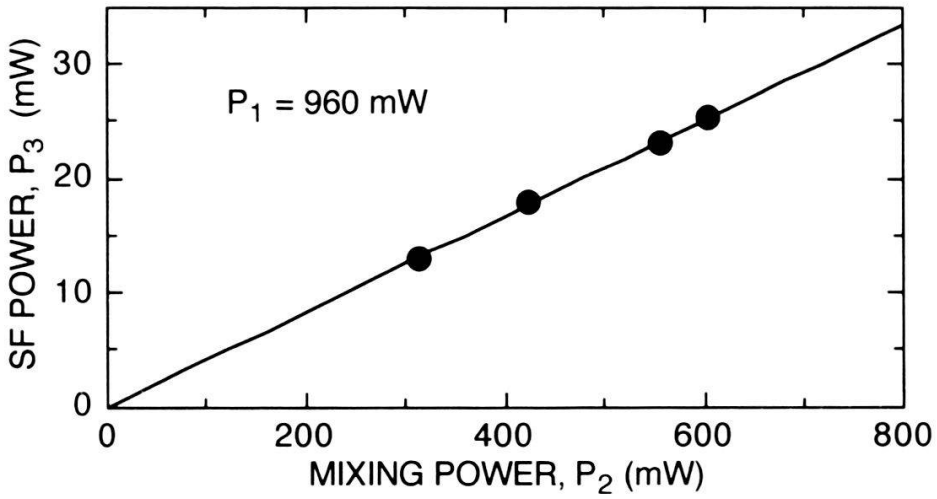

Fig. 1: Output power (•) of the 433 nm radiation as a function of the incident pump power at 774 nm from the AlGaAs laser diode for noncritical type I PM SFG with an overall conversion efficiency of 4.1 % (—).

In conclusion, we demonstrated a blue laser based on noncritical type I sum-frequency mixing of AlGaAs and InGaAs laser diodes in $KNbO_3$. An output power of 25 mW of diffraction-limited CW radiation was generated in a 6.6 mm long crystal. The blue laser was continuously tuneable from 431 to 438 nm.

References

1. I. Biaggio, P. Kerkoc, L.-S. Wu, P. Günter, B. Zysset, J. Opt. Soc. Am. B **9**, 507 (1992).
2. R. Parke, D. F. Welche, A. Hardy, R. Lang, D. Mehuys, S. O'Brien, K. Dzurko, D. Scifres, IEEE Photonics Technol. Lett. **5**, 297 (1993).
3. C. Zimmermann, V. Vuletic, A. Hemmerich, T. W. Hänsch, Appl. Phys. Lett. **66**, 2318 (1995).
4. D. Fluck, T. Pliska, P. Günter, Opt. Commun. **123**, 624 (1996).